A comparison between ab initio calculated and measured Raman spectrum of triclinic albite ($NaAlSi_3O_8$)

Irene Aliatis, [a,*] Erica Lambruschi,[a] Luciana Mantovani,[a] Danilo Bersani,[a] Sergio Andò,[b] G. Diego Gatta,[c] Paolo Gentile,[b] Emma Salvioli-Mariani,[a] Mauro Prencipe,[d] Mario Tribaudino,[a] Pier Paolo Lottici[a]

[a] *Università di Parma, Dipartimento di Fisica e Scienze della Terra, Parco Area delle Scienze 7/A, 43124 Parma, Italy. E-mail: irene.aliatis@difest.unipr.it*
[b] *Università di Milano Bicocca, Dipartimento di Scienze dell'Ambiente e del Territorio e di Scienze della Terra, Piazza della Scienza 4, 20126 Milano, Italy.*
[c] *Università degli Studi di Milano, Dipartimento di Scienze della Terra, via Botticelli 23, 20133 Milano, Italy.*
[d] *Università di Torino, Dipartimento di Scienze della Terra, via Valperga Caluso 35, 10125 Torino, Italy.*

Abstract

Albite is one of the most common mineral in the Earth's crust and its polymorphs can be found in rocks with different cooling histories. The characteristic pattern of vibration of the albite mineral reflects its structural Si/Al-ordering. In this study, we report on the comparison between the Raman spectra measured on a natural, and fully ordered (as deduced on the basis of single-crystal X-ray diffraction data), "low albite", $NaAlSi_3O_8$, and those calculated at the hybrid Hartree-Fock/Density Functional level by employing the WC1LYP Hamiltonian, which has proven to give excellent agreement between calculated and experimentally measured vibrational wavenumbers in silicate minerals. All the 39 expected A_g modes are identified in the Raman spectra and their wavenumbers and intensities, in different scattering configurations, well correspond to the calculated ones. The average absolute discrepancy $\overline{|\Delta\nu|}$ is ~ 3.4 cm^{-1}, being the maximum discrepancy $|\Delta\nu|_{max}$ ~ 10.3 cm^{-1}. The very good quality of the WC1LYP results allows for reliable assignments of the Raman features to specific patterns of atomic vibrational motion.

1. Introduction

Feldspars are the most abundant minerals in the Earth's crust, making up more than 60% of both the continental crust and the oceanic crust. Albite, $NaAlSi_3O_8$, is the sodic endmember of plagioclase [albite – anorthite ($CaAl_2Si_2O_8$) solid solution] and alkali-feldspars [albite – K-feldspar ($KAlSi_3O_8$) solid solution]. It is most common in granites, granodiorites, rhyolites and alkaline rocks such as syenite. In metamorphic rocks it is most common in low-grade pelitic rocks. It occurs within immature clastic sediments (Smith and Brown, 1988; Deer et al., 2001). Albite structure (Fig. 1) is built by of corner-sharing AlO_4 and SiO_4 tetrahedra linked in an infinite three-dimensional array. The basic building unit of its framework consists of rings of four tetrahedra (four symmetrically non-equivalent sites in the triclinic structure, designated as $T_1(0)$, $T_1(m)$, $T_2(0)$ and $T_2(m)$, and only two in the monoclinic one, i.e. T_1 and T_2) forming double crankshaft-like chains. The crankshaft chains are linked through adjacent T_2 vertices (O_A2 oxygens) in the *b* direction forming sheets of chains. Successive sheets of double crankshafts are linked through O_A1 oxygens in the *c* direction by T_1 tetrahedra pointing upwards and downwards, forming a plane of structural weakness, responsible for the good (001) cleavage in all feldspars. The O_A2 atoms are located on (010) mirror or pseudo-mirror planes, whereas O_A1 oxygen atoms lie on two-fold axis or pseudo-two-fold axis. T_2 tetrahedra have bonds only within the sheets, connecting the crankshafts, whereas T_1 tetrahedra link the sheets: each T_2 tetrahedron is therefore joined by

one T_2 and three T_1 tetrahedra, and each T_1 tetrahedron by one T_1 and three T_2 tetrahedra. The 3D structure forms tetrahedral cages with Na^+ ions lying in the cavities (Smith, 1974; Ribbe, 1983; Angel et al., 2012). The Na^+ cations are located between the (001) slabs and lie exactly on the (010) mirror plane in monoclinic feldspars or very near the pseudo-mirror planes in triclinic feldspars. The weakness of the bonds to these 6- to 9- coordinated cations, compared with those to the 4-coordinated Al and Si atoms, is responsible for the excellent (010) cleavage in feldspars. In albite, Al atoms occupy the $T_1(0)$ tetrahedral site of the four-membered tetrahedral rings in the ordered structure, known as "low albite" (triclinic, space group $C\bar{1}$). Albite exhibits also three different high-temperature polymorphs, where Al and Si are statistically distributed between the tetrahedral sites and the complete ordering is lost. *Monoalbite* (MA) is the monoclinic polymorph, which forms from the triclinic-to-monoclinic phase transition at 980 °C and 0.0001 GPa of disordered albite; *analbite* (AA) is the triclinic polymorph, essentially completely disordered under 980 °C (at 0.0001 GPa), which transforms to monoalbite on heating; *high albite* (HA) is a further triclinic polymorph, resulting from the diffusive ordering in the (Si-Al) distribution (Ribbe, 1983). Albite occurs in rocks mainly as low albite; this is because Ab-rich feldspars are rare in rapidly cooled rocks, and in more slowly cooled rocks, ordering rates in such feldspars are fast compared to cooling rates (Brown and Parson, 1989). A series of studies have been devoted to the thermodynamics of alkali feldspars (*e.g.*, Carpenter 1988; Salje 1985, 1986; Salje et al. 1985). The characteristic pattern of vibration of the albite mineral reflects its structural Si/Al-ordering, which in turn reflects the physical-chemical conditions of the hosting rock.
The aim of this study is the *ab initio* calculation of the Raman spectrum (wavenumbers and intensities) of low albite following the same approach successfully used for other minerals (Prencipe et al., 2004; Prencipe et al., 2006; Prencipe et al., 2009; Prencipe et al., 2012; Stangarone et al., 2014; Prencipe et al., 2014). The reliability of the results depends on several factors and computational details, including the correct choice of the Hamiltonian for the studied mineral (De La Pierre et al., 2011; Prencipe et al., 2012). The calculation of the Raman intensities is essential for a correct and unambiguous assignment of the eigenmodes to the corresponding measured features, especially in complex silicates, such as open-framework silicates, where overlapping modes within narrow spectral ranges are very frequent. In the following, the computed wavenumbers and intensities will be compared with the results of Raman scattering measurements on an albite crystal in different crystallographic orientations, with the goal to assign each peak to specific patterns of atomic vibrational motions. In line with this study, further comparative *ab initio* simulations and Raman experiments on alkali feldspars with different tetrahedral ordering are in progress.

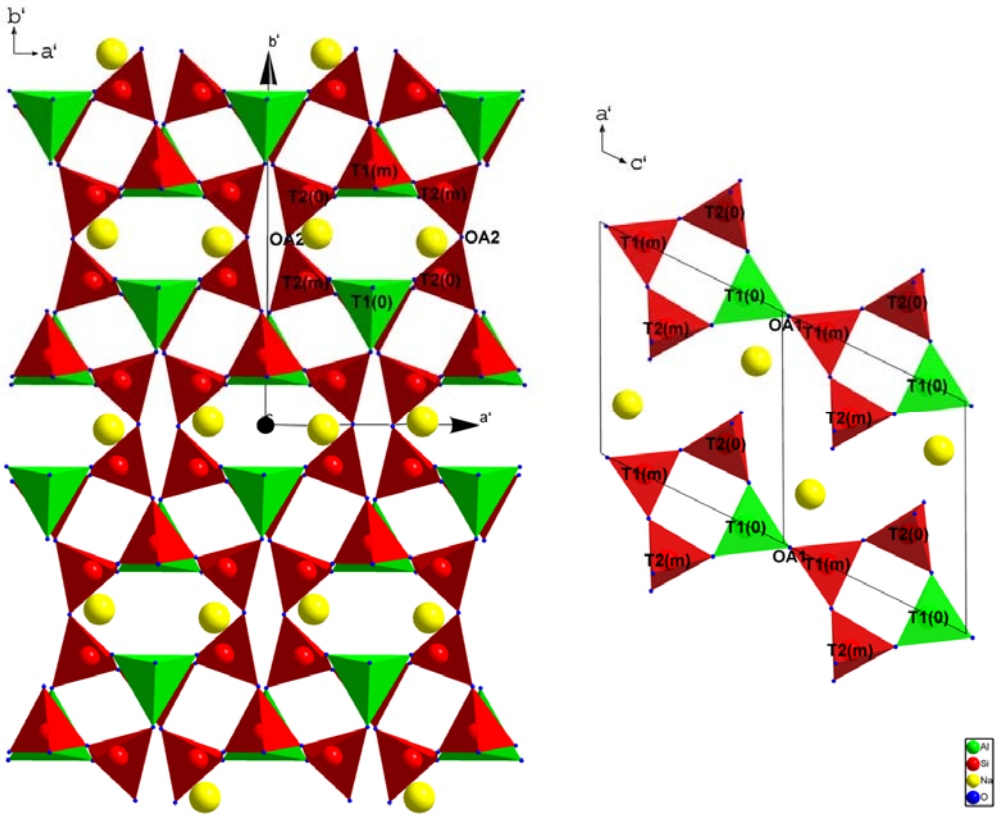

Fig. 1: Albite structure (*left*: *c* axis projection; *right*: *b* axis projection) obtained by the single-crystal X-ray structure refinement of the studied sample. The red tetrahedra contain silicon, the green ones aluminum, Na^+ atoms are shown in yellow. The four non-equivalent tetrahedra are labeled as $T_1(0)$, $T_1(m)$, $T_2(0)$ and $T_2(m)$. The two types of oxygens (O_{A1} and O_{A2}) are shown too.

2. Materials and methods

2.1 Sample characterization

The albite sample used in this study comes from Minas Gerais, Brazil. Phase identification of the sample was performed by powder X-ray diffraction (Bruker D2 diffractometer). Chemical analyses (Tescan Vega TS 5136 XM scanning electron microscope, equipped with an EDAX Genesis 4000 JXM EDS spectrometer) indicate an almost end-member composition (Table 1), with K_2O and CaO concentrations of 0.32 and 0.19 wt%, respectively. The unit-cell constants (Table 2) were measured by single-crystal X-ray diffraction (Xcalibur diffractometer equipped with CCD and Mo$K\alpha$ radiation). The order parameter, Q_{od}, which defines the degree of Al/Si order relative to completely ordered albite, is 1.0. It is calculated as $Q_{od} = (t_{1(0)} - t_{1(m)})/(t_{1(0)} + t_{1(m)})$, with the site occupancies t_i obtained from the average bond distances for each tetrahedron, determined by single-crystal structure refinements, as $t_i = 0.25(1 + n_{An}) + (< \mathrm{T_i} - O > - \ll T - O \gg)/0.135$ (Tribaudino et al., 2010), where t_i is the number of Al atoms occupying T_i tetrahedra divided by the number of tetrahedra and n_{An} is the molar fraction of anorthite content. $< T_i - O >$ is the mean of four (Si, Al)-O bond lengths for each tetrahedron, and $\ll T - O \gg$ is the grand mean of all non-equivalent $T - O$ bond lengths in the unit cell.

2.2 Computational method

Geometry optimization and spectral calculations on low albite were performed by using the CRYSTAL14 program (Dovesi et al., 2013), which employs localized basis sets. Computations were made at the hybrid Hartree-Fock/Density Functional level (HF/DFT) employing the WC1LYP (Lee et al., 1988; Wu and Cohen, 2006) exchange-correlation functional, which includes a percentage (16%) of the exact non-local Hartree-Fock exchange in order to correct for the self interaction error (SIE; the interaction of an electron with itself) which is typical of purely DFT LDA or GGA functionals. The use of hybrid HF/DFT functionals has been demonstrated to be crucial for a reliable calculation of Raman shifts or more in general, for the calculation of the wavenumbers of vibrational modes in crystals (Prencipe et al., 2009; Demichelis and Civalleri, 2010; De La Pierre et al., 2011; Prencipe et al., 2012).

The atomic basis sets employed were from the CRYSTAL online library at the address www.crystal.unito.it/basis-sets.php. More precisely, they were: 8-511G(1d) for Na; 8-511G(1d) for Al; 88-31G(2d) for Si, and 8-411G(2d) for O, where the symbols 1d and 2d stand for the presence of one and two polarization functions, respectively. The grid for the evaluation of the DFT exchange-correlation functionals was chosen by the keyword XXLGRID of the CRYSTAL14 User Manual (Dovesi et al., 2013) and corresponds to a total of 631097 points in the (primitive) unit cell. A measure of the excellent numerical accuracy provided by such a grid is the evaluation of total number of electrons in the unit cell, by the numerical integration of the electron density over the cell volume: 259.999995 electrons out of 260.

The thresholds controlling the accuracy of the calculation of Coulomb and exchange integrals were set to 8 (ITOL1 to ITOL4) and 18 (ITOL5 (Dovesi et al., 2013)). The diagonalization of the Hamiltonian matrix was performed at 36 independent **k** vectors in the reciprocal space (Monkhorst net (Monkhorst and Pack, 1976)) by setting to 4 the shrinking factor IS (Dovesi et al., 2013).

Cell parameters and fractional coordinates were optimized by analytical gradient methods, as implemented in CRYSTAL14 (Civalleri et al., 2001; Dovesi et al., 2013). Geometry optimization was considered converged when each component of the gradient (TOLDEG parameter in CRYSTAL14) was smaller than 0.00003 hartree/bohr and displacements (TOLDEX) were smaller than 0.00012 bohr with respect to the previous step.

The calculated equilibrium lattice parameters optimized at the WC1LYP level (static values: no zero point and thermal effects included; see below) are reported in Table 2 (column "a"). Zero point and thermal pressures at 300 K, and their impact on the calculated structure of low albite were estimated by calculating the full vibrational spectrum at the Γ point at different unit cell volumes, according to the procedure described by Prencipe et al. (2011). Cell parameters at 300 K are reported in Table 2 (column "b"). The calculation also provided an estimation for the bulk modulus (K_0) of low albite of 54.1 GPa at 300 K ($\partial K_0/\partial P = K' = 6.4$), from the fit of a third-order Birch-Murnaghan (Birch, 1966) equation of state to the computed pressure-volume data in the [0 - 7 GPa] pressure range. These elastic parameters are in excellent agreement with the experimental findings of Benusa (2005), who reported a K_0 of 54.2(7) GPa ($K' = 5.3()$), at least in the low pressure range. As usual with DFT calculations at the GGA level (even in the case of hybrid functionals like WC1LYP), the cell parameters and volumes are somewhat overestimated with respect to the experimental data.

The optimized structure at the cell volume of 680.23 Å^3 (Table 2, column "b"), corresponding to the calculated geometry of low albite at 300 K (zero point effects included), is the one employed in the calculation of the Raman shifts discussed in the subsequent sections.

The Raman shifts (*i.e.* the wavenumbers of the Raman-active modes) are calculated as the eigenvalues of the matrix of the second derivatives of the full potential of the crystal with respect to the mass-weighted nuclear displacements (Hessian matrix) (Pascale, 2004); as a *by-product* of the calculation, the eigenvectors matrix is obtained, whose columns represent the normal modes in the basis of the mass-weighted nuclear coordinates.

Relative intensities of the Raman signals are computed using a fully analytical approach (Maschio et al., 2012; Maschio et al., 2013) formulated and implemented in the CRYSTAL14 program. The computed Raman intensities refer to the experimental conditions $T = 300$ K, $P = 1$ atm and $\lambda = 632.8$ nm, as laser excitation line.

The attribution of each mode to the pattern of motion of the atoms of the structure was made by direct inspection of the eigenvectors and their components (on the basis of the weighted atomic coordinates) and can be visualized by looking at animations of the normal modes generated on the basis of such eigenvectors (Moldraw software, *http://www.moldraw.unito.it/_sgg/f10000.htm*). To help in the determination of the nature of the vibrational modes, the isotopic shifts induced by changes in the cation masses were calculated. The isotopic shift is a general tool useful to understand the contribution of the various ions in each normal mode, and it can be generated at essentially no additional computational cost in the simulation, just by changing by some amount (about 20% in our case) the masses of different nuclei in the structure. Such procedure was followed for Na, Al and Si.

2.3 Experimental method

Raman spectra have been collected by a Horiba Jobin-Yvon LabRAM apparatus in backscattering geometry. The spectrometer (300 mm focal length) is equipped with an Olympus BX40 confocal microscope with objectives up to 100X and a motorized x–y stage. A He-Ne laser at 632.8 nm (maximum power 20 mW) was used for excitation. The Rayleigh radiation was blocked by reflective volume Bragg grating notch filters BragGrate™ (OptiGrate), which enable Raman measurements 5-10 cm^{-1} from the laser line. The backscattered Raman light was dispersed by a 1800 grooves/mm holographic grating onto a Peltier cooled CCD (1024x256 pixels). The entrance slit width was fixed at 150 μm.

Raman spectra have been collected on (010), (001) and (100) crystallographic faces of the crystal, properly cut. Samples were mounted on a goniometric stage and oriented under the 50X ULWD objective (NA = 0.55, WD = 8 mm, lateral spatial resolution = 2 μm) as follows:

- (010) face: the incident beam polarization was made to correspond to the *a* crystallographic axis, which is easily recognizable as the cleavage traces on this face are parallel to *a* axis;
- (001) face: the *a* crystallographic axis is parallel to the edge between (010) and (001) faces. The laser polarization was made again to coincide with the *a* axis;
- (100) face: the incident beam is approximately along the *a* axis, hence the laser polarization was made to correspond with the *b* axis.

The direction of the laser polarization on the three aforementioned faces was used to set the Raman spectrum taken at θ = 0°. On each face measurements were collected at θ = 0° and θ = 90°.

Directional Raman measurements have been collected in parallel and cross polarizations: XX, ZZ and XZ independent components of the Raman tensor were collected on (010) face, rotating the crystal from θ = 0° up to θ = 90°; YY and XY components were measured on (001) face, whereas ZZ and YZ components on (100) face. We assumed the laboratory $X_{lab}Y_{lab}Z_{lab}$ frame coinciding with the Cartesian orthogonal system XYZ as given by CRYSTAL.

For a complete definition of the orientation of the lattice with respect to the Cartesian frame XYZ, the three direct lattice vectors of the primitive unit cell are defined as follows (the standard crystallographic orientation is used): $\mathrm{a} = +4.1\,X + 6.5\,Y + 0.0058\,Z;\ \mathrm{b} = -4.1\,X + 6.2\,Y - 0.0075\,Z;\ \mathrm{c} = -3.2\,X - 0.5\,Y + 6.4\,Z$. Moreover, the angles (°) between the XYZ Cartesian axes and the *a b c* crystallographic axes (shown in Fig. 2) are given by the matrix:

2.31450	89.95841	116.47062
87.68734	0.04229	94.25207
89.90773	90.00767	26.86330

X axis forms an angle of about 2° with the *a* crystallographic axis, Y axis is (nearly) taken as the *b* crystallographic axis and Z axis is nearly perpendicular to the *ab*-plane at ~ 26° from the *c*-axis.

Typical exposures of the Raman measurements were 60-180 seconds, repeated 3-6 times. The system was calibrated on the silicon Raman peak at 520.6 cm^{-1}. Spectra were collected in the range 50-1200 cm^{-1} with a spectral resolution of about 1 cm^{-1}. The baseline subtraction with a 2nd degree polynomial curve and the peak fitting were made with LABSPEC 5.78.24 software package, Jobin Yvon/Horiba, subdividing each spectrum in four spectral ranges.

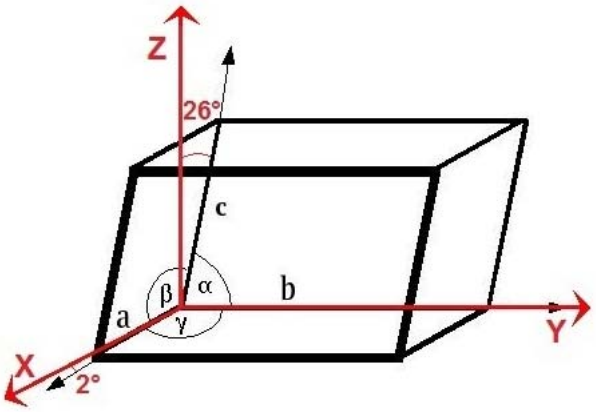

Fig. 2: Raman tensor XYZ axes with respect to the triclinic crystallographic cell (*a b c* crystallographic axes).

3. Results

The structure of low albite is generally described in a non-standard space group $C\bar{1}$ in order to preserve the axial orientations among the feldspar group of minerals, though a primitive cell $P\bar{1}$ could be used (Ribbe, 1983). Either the Al, Si and Na cations, or the O anions sit on the *2i* Wyckoff positions. The number of atoms for the primitive cell is 26 (13 atoms per formula unit, Z = 2), giving rise to 78 different vibrational modes. The symmetry decomposition at **k** = 0 of the normal modes in the C_i point group of albite is:

$\Gamma_{tot} = 39\ A_g + 39\ A_u$,

out of which: 3 A_u modes correspond to the rigid translations of the whole crystal, 36 A_u modes are IR active, whereas the 39 A_g ones are Raman active. The expected 39 Raman modes wavenumbers and their relative intensities, computed by CRYSTAL software, as well as our experimentally determined wavenumbers are listed in Table 3.

3.1 Comparison of our simulation and experiment

In this section, we provide a comparative analysis of our simulated and experimental Raman spectra. The wavenumbers of all the 39 expected A_g modes are in very good agreement with those measured in our spectra (see Table 3): the mean absolute difference $\overline{|\Delta\nu|}$ over the 39 modes is 3.4 cm^{-1}. The largest differences ($\Delta\nu \sim 10\ cm^{-1}$) are due to the modes #21 (466 cm^{-1}) and #31 (825 cm^{-1}).

To give a rough picture of the agreement between *ab initio* calculations and experimental results, in Fig. 3 the simulated spectrum for a polycrystalline isotropic sample, at excitation wavelength of 632.8 nm and temperature of 300 K, and assuming an overall Lorentzian broadening of 8 cm^{-1}, is compared with an experimental spectrum obtained by averaging the spectra taken on the three different faces of the crystal (*i.e.* (010), (001) and (100)), in two different orientations (0° and 90°). We may observe a fairly well agreement for wavenumbers and intensities of the Raman features. A closer comparison between computed and experimental Raman spectra allows a

reliable characterization of doubtful modes. The broad band centered at ~ 68 cm^{-1} is a convolution of the modes #1 and #2; six Raman bands corresponding to the modes from #5 to #10 have been resolved in the range 130 and 190 cm^{-1}, where the measured spectrum shows two maxima centered at 162 and 185 cm^{-1} and two shoulders at 149 and 169 cm^{-1}, respectively. The mode #21, calculated at 466 cm^{-1} and measured at 456 cm^{-1}, is observed (with medium intensity) only in the spectra collected on (001). The broad bands around 1000 cm^{-1} and 1040 cm^{-1} are due to the overlap of the modes #33-#34 and #35-#36, respectively; the strong Raman band at 1099 cm^{-1} and its shoulder at 1115 cm^{-1} correspond to the modes #37 and #38. On the contrary, the very weak mode #23, computed at 492 cm^{-1}, cannot be resolved between the two strong bands observed at 478 cm^{-1} and 507 cm^{-1}.

A more significant comparison may be made referring to the single components of the Raman tensor. The 39 A_g modes give non-vanishing XX, YY, ZZ, XY, YZ and XZ components of the Raman tensor. In Fig. 4, we report the six independent single-crystal directional spectra obtained from our calculations in comparison with the experimental ones. The six measured spectral profiles agree very well with the simulated ones. Some leakage is obviously present: for example, in the XY spectrum the strongest A_g modes at 478 cm^{-1} and 507 cm^{-1} are still observed even though, according to the selection rules, they should have negligible intensities.

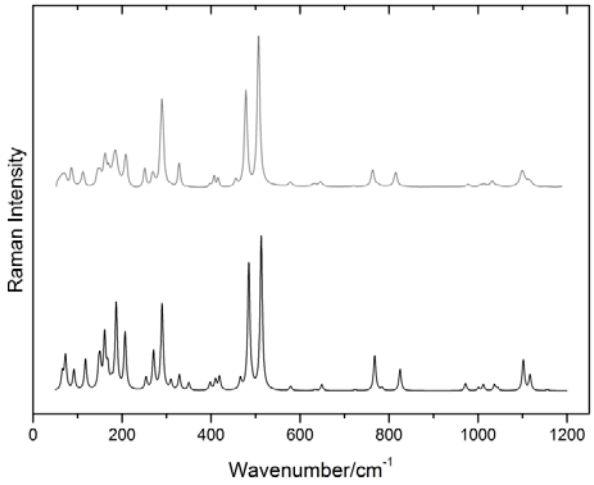

Fig. 3: Experimental averaged Raman spectrum of albite (in gray) compared with the simulated spectrum (in black) for polycrystalline isotropic powder, calculated at 632.8 nm wavelength and 300 K.

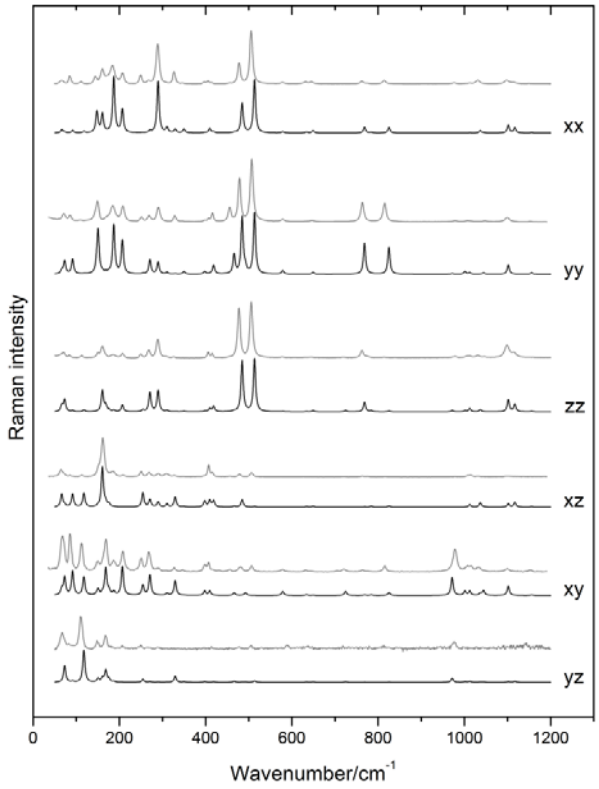

Fig. 4: Calculated Raman spectra of albite for the six different polarization configurations (in black) compared with the experimental data (in grey). Each measured spectrum is scaled so that the intensity of the strongest peak agrees with the theoretical intensity of the corresponding calculated mode.

4 Discussion

4.1 Review and discussion of experimental data

In the last 40 years, several research groups have measured and studied the Raman spectra of feldspars. Several sets of experimental data are available in recent literature for the Raman active modes of albite. First, in 2005, McKeown (2005) classified the full set of 39 symmetry allowed modes. He reported the unpolarized Raman spectrum of a triclinic crystal of ordered albite at room temperature and studied the evolution of the Raman features from 25 °C to above the melting temperature at 1118 °C, by *in situ* disordering through the triclinic-to-monoclinic displacive phase transition. In 2008, Bendel and Schmidt (2008) used the assignments made by McKeown (2005) and suggested a method for the determination of the Na/K ratio in disordered alkali feldspars along the join $KAlSi_3O_8$ and $NaAlSi_3O_8$ by the wavenumbers of three Raman bands located in range 120-142 cm^{-1}, 454-461 cm^{-1} and 510-514 cm^{-1}, respectively. In the same year, Freeman et al. (2008) prepared a database, based on a large number of natural feldspar-group minerals, able to classify ten types of feldspars according to their structure, crystallinity and chemical composition solely on the basis of their Raman spectra. Once again, the assignments were based on the calculations of McKeown (2005), and five groups of feldspar spectral characteristics were attempted. McKeown (2005) displayed all the 39 A_g modes of albite, whereas Freeman et al. (2008) listed only 28 modes for low albite and 24 modes for high albite (their experimental results are reported in Table 3). Our measured Raman wavenumbers well correspond to those reported by McKeown (2005), except for the features at 216, 367, 528 and 1070 cm^{-1} which are absent in our spectra. Besides, two

wavenumbers are counted twice (*i.e.* 346 and 720 cm^{-1}) (McKeown, 2005). Therefore, six of our observed Raman wavenumbers do not have a corresponding feature in the Raman spectra reported by McKeown (2005). On the contrary, all the 28 Raman bands listed by Freeman et al. (2008) are also detected in our spectra with a good correspondence: the largest discrepancies in the wavenumbers are found for the high albite (second column), being a disordered sample.

Moreover, the main Raman features of 7 different albite samples are described in Freeman et al. (2008) and four Raman characteristic bands for a Na-rich sample are reported in Bendel and Schmidt (2008). A comparative analysis of these data in Table 4 suggests again that our main experimental wavenumbers are in good agreement with those measured by Freeman et al. (2008) and McKeown (2005), whereas major differences are found with respect to Bendel & Schmidt (2008) results. All the samples mentioned in Table 3 and 4 are albites with chemical composition very close to the Na-endmember. In particular, the albite of McKeown (2005), found in Rutherford Mine in Amelia (Virginia), is very similar in composition (K_2O and CaO concentrations were found to be 0.29 and 0.0 wt%, respectively) and in structure to our sample. Samples described in Freeman et al. (2008) have an albite content ranging from 93.66 up to 100%. The only synthetic sample (Bendel and Schmidt, 2008), listed in Table 4, is a disordered albite (analbite) produced from a natural gem-quality sanidine megacryst from Volkesfeld by ion exchange at about 850 °C in molten NaCl (following the method described in Kroll et al. (1986). Its structural and compositional disorder could explain the large differences in peak positions.

4.2 Review and discussion of calculated data

First normal mode calculations for the alkali feldspars albite, microcline and sanidine, based on a valence force potential model, were performed in 1977 by von Stengel (1977): the Raman- and IR-mode frequencies were reported, but no vibrational assignment was attempted. In 2005, a similar approach, based on lattice dynamics (LD) calculations, was repeated by McKeown (2005) and a detailed description of each mode was also presented (McKeown, 2005). These procedures are, however, not fully satisfactory since, apart from being based on classical models of atomic interactions, require the *a priori* knowledge of which modes are fundamentals and which are not. To the best of our knowledge, the most recent paper on albite calculations was published in 2014 by Méheut & Schauble (2014). They determined the isotope fractionation factors for oxygen and silicon in phyllosilicates (pyrophyllite, talc), albite and pyrope, from harmonic partition functions, which require the knowledge of the phonon frequencies, using first-principles methods based on density functional theory (PBE functional).

Table 5 compares our calculated Raman frequencies with those presented in the aforementioned works (McKeown, 2005; Méheut and Schauble, 2014). Overall, all the authors computed 39 Raman modes, out of which 33 are common. Six frequencies (*i.e.* 221, 349, 362, 526, 728 and 1173 cm^{-1}), computed by McKeown (2005) are not expected both in our and in Méheut & Schauble (2014) calculated data. In particular, the simulation from McKeown (2005) provided two doublets, at 344 and 349 cm^{-1}, and at 725 and 728 cm^{-1}, respectively, which are unresolved in the Raman spectrum and attributed to the experimental features at 346 and 720 cm^{-1}, respectively. Five Raman frequencies are present only in our and in PBE (Méheut and Schauble, 2014) calculations, but the differences are very large (up to 46 cm^{-1}), except for the mode at 176 cm^{-1}.

The first column in Table 5 reports also measured frequencies at 414, 770 and 1010 cm^{-1} (in bold), attributed by McKeown (2005) to overtones, which Méheut and Schauble (2014) calculate (± 17-44 cm^{-1}) as fundamental modes. The fundamental nature of the aforementioned bands is supported by our calculation, which gives normal modes at 419, 784 and 1012 cm^{-1}, respectively. The computed frequency at 60 cm^{-1} by Méheut and Schauble (2014) does not correspond to any mode in our computation. Further, the frequency at 73 cm^{-1}, expected in all the calculations, has not been assigned to the same observed band. These discrepancies are due to the fact that McKeown (2005) observed only two bands at low wavenumbers (*i.e.* 67 and 89 cm^{-1}), instead of three (*i.e.* 63, 72 and 86 cm^{-1}). Our calculated Raman modes at 66 and 73 cm^{-1} should then be compared with those by Méheut and Schauble (2014) at 60 and 73 cm^{-1}, respectively.

4.3 Analysis of the normal modes

Consistently with the previous work by Freeman et al. (2008) our calculated 39 normal modes can be approximately classified in five groups: Group I (in the range 450 and 520 cm^{-1}) is characterized by the two strongest peaks due to the breathing modes of the four-membered tetrahedral rings; Group II (200-400 cm^{-1}) and Group III (below 200 cm^{-1}) include bands due to rotation-translation modes of the rings and cage-shear modes, respectively; Group IV (600-900 cm^{-1}) describes the deformation modes of the tetrahedra, whereas Group V (900-1200 cm^{-1}) is characterized by the vibrational stretching modes of the tetrahedra.

From the analysis of the eigenvectors and by looking at animations of the corresponding normal modes, the attributions, made by McKeown (2005) and Méheut and Schauble (2014), have been revised as follows (we report here only a short description of the main contributions to the atomic movements):

Below 200 cm^{-1}: cage-shear modes

1) mode at 66 cm^{-1}: mainly translation of the Na^+ cations along the *a* direction, accompanied by rigid rotations of the SiO_4 tetrahedra;
2) mode at 73 cm^{-1}: translation of the Na^+ cation parallel to the *a* axis;
3) mode at 92 cm^{-1}: similar to the A_g mode at 66 cm^{-1}, but the AlO_4 tetrahedra are also involved;
4) modes at 118 and 148 cm^{-1}: rotations of the four non-equivalent tetrahedra, accompanied by the translation of Na^+ cations, whose contribution to the motion is higher at 148 cm^{-1} than at 118 cm^{-1};
5) modes at 151, 161 and 168 cm^{-1}: Na translations and rigid translations of the tetrahedra (tetrahedral cages deformations);
6) modes at 176 and 187 cm^{-1}: mainly associated to the Na^+ cations translations in the tetrahedral cages: parallel and perpendicular to the *b* axis, respectively;
7) mode at 207 cm^{-1}: rigid translation of the tetrahedra, accompanied by the Na^+ motion along the *b* direction;

200-400 cm^{-1}: rotation-translation modes of the rings

8) mode at 254 cm^{-1}: rigid rotations of the SiO_4 tetrahedra and deformation of the AlO_4 tetrahedra, where the Al and O atoms move significantly;
9) modes at 271 and 290 cm^{-1}: rotations of the tetrahedra (see as an example the mode at 290 cm^{-1} in Fig. 5);
10) modes at 310, 329, 350, 398, 410 and 419 cm^{-1} are mainly associated with the deformations of the tetrahedra (mainly bending modes of the Al-O-Si and Si-O-Si bonds);

400-520 cm^{-1}: ring-breathing modes

11) mode at 466 cm^{-1}: deformation of the tetrahedra; Si atoms contribute to the motion, in particular in the $T_2(0)$ tetrahedra;
12) modes at 485 (in Fig. 5) and 490 cm^{-1}: deformations of the tetrahedra, mainly O-Si-O and Si-O-Si (or Al) bending. The first one is a clear cage breathing mode. The deformation of the Si- tetrahedra is higher than the Al-tetrahedra, as suggested by the calculated isotopic shifts of the wavenumbers when Al and Si masses are increased by ~ 20% (see Fig. 6),
13) mode at 513 cm^{-1}: bending deformation of the Al-O-Si and Si-O-Si bonds, with the central cations of the tetrahedra almost stationary (see Fig. 5);

600-900 cm^{-1}: deformation modes

14) mode at 579 cm^{-1}: deformation of the tetrahedra, with a strong contribution of $T_1(m)$;
15) modes at 634, 649 and 724 cm^{-1}: mainly bending-deformation of the tetrahedra, where the contribution of the aluminum to the movement is predominant in modes at 634 and 724 cm^{-1};
16) mode at 768 cm^{-1}: bending deformation of $T_2(m)$ tetrahedra;

17) modes at 784 cm^{-1} and 825 cm^{-1} (Fig. 5): deformation of the four tetrahedra. The $T_i(0)$ tetrahedra give a major contribution to the motion at 784 cm^{-1};

900-1200 cm^{-1}: vibrational stretching modes

18) mode at 972, 1001 and 1012 cm^{-1}: stretching of the T_2 tetrahedra;
19) mode at 1037 cm^{-1} : stretching of $T_2(m)$ tetrahedra;
20) mode at 1044 cm^{-1}: mainly anti-symmetric stretching of the $T_1(m)$ and $T_2(m)$ tetrahedra;
21) mode at 1102 cm^{-1}: anti-symmetric stretching for all the SiO_4 tetrahedra;
22) mode at 1117 cm^{-1}: anti-symmetric stretching of the $T_1(m)$ and $T_2(o)$;
23) mode at 1156 cm^{-1}: symmetric stretching of the $T_i(m)$ tetrahedra.

The calculated isotopic shifts of the wavenumbers of albite helps estimating the contribution of the different cations to the modes. As shown in Fig. 6, the Na^+ cations contribute only to the modes below 210 cm^{-1}, whereas the contribution of Al is predominant mainly in the spectral range of the Group IV and Si is most involved above 400 cm^{-1}. The specific contribution of the cations differs with respect to previous assignments (McKeown, 2005; Méheut and Schauble, 2014). In addition, in Fig. 6 upper panel, the contribution of Si in the three non-equivalent tetrahedra may be recognized: $T_1(m)$, $T_2(o)$ and $T_2(m)$ are randomly involved in the majority of the Raman peaks.

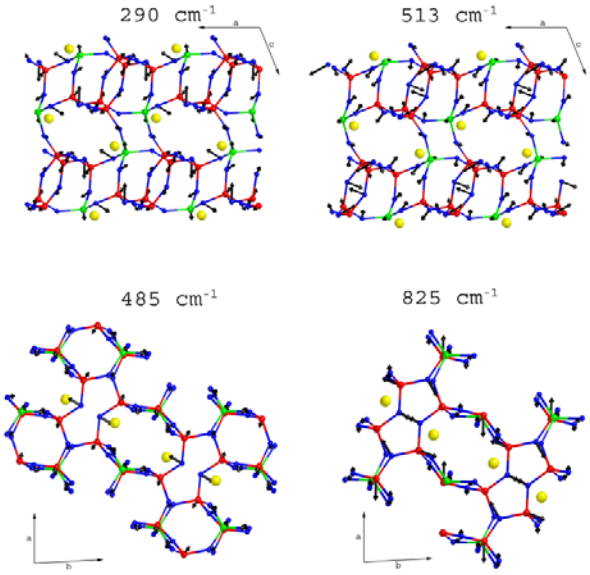

Fig.5: Eigenmode plots for four characteristic peaks in the Raman spectrum of albite: modes at 290 and 513 cm^{-1} are shown on *ac* plane, whereas modes at 485 and 825 cm^{-1} are displayed on *ab* plane. Atom displacements are indicated by black arrows. Atom types are: Na (yellow), Si (red), Al (green) and O (blue).

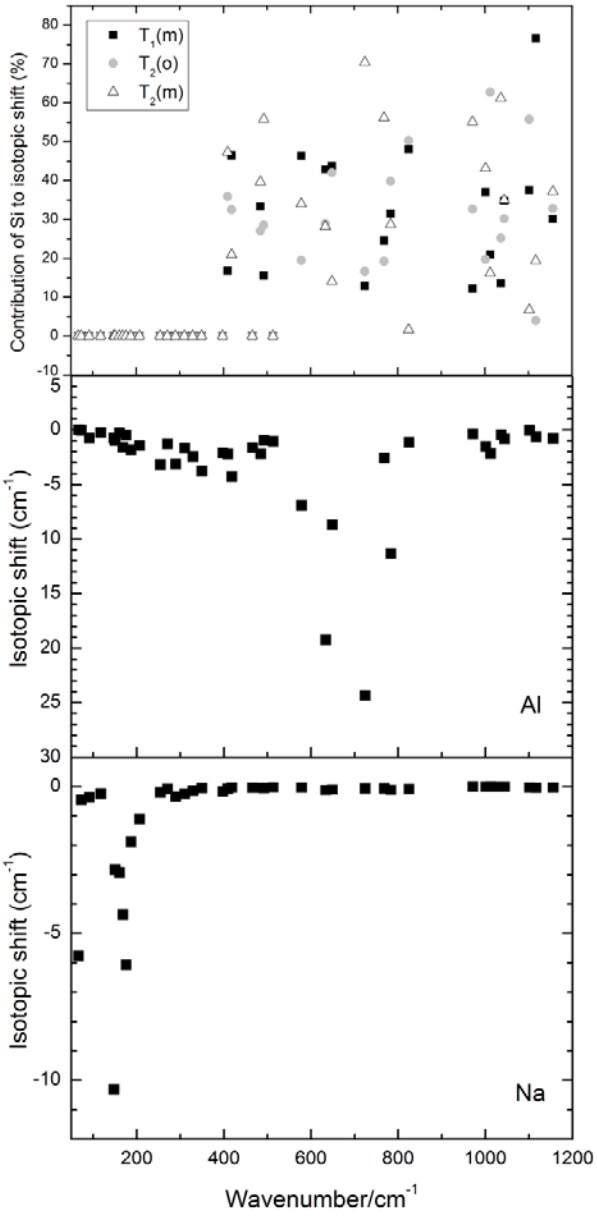

Fig. 6: Calculated isotopic shift of the wavenumbers of albite when Na (lower panel) or Al (middle panel) mass is increased by ~ 20%. In the upper panel is reported the percentage contribution of Si, calculated from its different isotopic shifts in the three occupied atomic position (Taylor, 1933).

5 Conclusion

The *ab initio* simulation method at the DFT level with the WC1LYP functional of low albite provides excellent agreement between calculated and experimentally measured Raman vibrational wavenumbers and intensities. In particular, the Raman spectra obtained in six different scattering geometries agree fairly well with the computed Raman tensor. New and reliable assignments to specific patterns of

atomic vibrational motions are now provided, solving some discrepancies reported in recent literature. Na, Al and Si isotope shifts help in identifying the modes in which the cations participate significantly. The recognition of the all 39 computed Raman modes in the experimentally measured spectra of the fully-ordered low albite, along with the detailed description of each vibrational motion, are essential to extend the comparative analysis to the different structural forms in which albite can be found, which reflect the physical-chemical conditions of the hosting rocks. We will perform further comparative *ab initio* simulations and Raman experiments on alkali feldspars with different tetrahedral ordering. Overall, the present study shows that the accurate *ab initio* simulation by CRYSTAL code provides a complete characterization of the Raman spectrum for triclinic crystalline compounds with many active modes (39 in the present case) being a very useful tool to complement experiment.

Acknowledgements

One of the authors (I.A.) is indebted to Fondazione Cariparma, Parma, for financial support. GDG acknowledges the Italian Ministry of Education (MIUR grant n. 2008SPZ743). This work was supported by MIUR grant n. 2010EARRRZ_005 (PRIN2010) "Dalle materie prime del sistema terra alle applicazioni tecnologiche: studi cristallochimici e strutturali" .

Brown, W. L., and Parsons, I. (1989) Alkali feldspars: ordering rates, phase transformations and behaviour diagrams for igneous rocks. Mineral. Mag., 53, 25-42.

Carpenter, M. A. (1988) Thermochemistry of aluminium/silicon ordering in feldspar minerals. In "Physical properties and thermodynamic behaviour of minerals" (Salje, E.H.K., ed.), NATO ASI Series C225, Reidel, Dordrecht, p. 265-323.

Salje, E. (1985) Thermodynamics of sodium feldspar I: Order parameter treatment and strain induced coupling effects. Phys. Chem. Minerals 12, 93-98.

Salje, E. (1986) Raman spectroscopic investigation of the order parameter behaviour of hypersolvus alkali feldspar: Displacive phase transition and evidence for Na-K site ordering. Phys. Chem. Minerals 13, 340-346.

Salje, E., Kuscholke, B., Wruck, B., and Kroll, H. (1985) Thermodynamics of sodium feldspar II: Experimental results and numerical calculations. Phys Chem Minerals Phys. Chem. Minerals 12, 99-107.

References

Angel R. J., Sochalski-Kolbus L. M. and Tribaudino M. (2012) Tilts and tetrahedra: The origin of the anisotropy of feldspars. *Am. Mineral.* **97**, 765–778. Available at: http://ammin.geoscienceworld.org/cgi/doi/10.2138/am.2012.4011.

Bendel V. and Schmidt B. C. (2008) Raman spectroscopic characterisation of disordered alkali feldspars along the join KAlSi₃O₈–NaAlSi₃O₈: application to natural sanidine and anorthoclase. *Eur. J. Mineral.* **20**, 1055–1065. Available at: http://openurl.ingenta.com/content/xref?genre=article&issn=0935-1221&volume=20&issue=6&spage=1055 [Accessed March 20, 2014].

Benusa, M.T., Angel, R.J., and Ross, N.L. (2005) Compression of albite, NaAlSi3O8. *Am. Mineral.* **90**, 1115–1120. Available at: http://ammin.geoscienceworld.org/cgi/doi/10.2138/am.2005.1805 [Accessed October 22, 2014].

Birch F. (1966) Compressibility, elastic constants. In *Handbook of physical constants* (ed. S. P. Clark). Geol. Soc. Am. Mem. pp. 97–174.

Civalleri B., D'Arco P., Orlando R., Saunders V. R. and Dovesi R. (2001) Hartree–Fock geometry optimisation of periodic systems with the Crystal code. *Chem. Phys. Lett.* **348**, 131–138. Available at: http://linkinghub.elsevier.com/retrieve/pii/S0009261401010818.

Deer W. A., Howie R. A. and Zussman J. (2001) *An Introduction to Rock-Forming Minerals*. 2nd ed., The Geological Society, Bath (UK).

Demichelis R. and Civalleri B. (2010) On the performance of eleven DFT functionals in the description of the vibrational properties of aluminosilicates. *Int. J. Quantum Chem.* **110**, 406–415. Available at: http://onlinelibrary.wiley.com/doi/10.1002/qua.22301/full [Accessed October 22, 2014].

Dovesi R., Saunders V. R., Roetti C., Orlando R., Zicovich-Wilson C. M., Pascale F., Civalleri B., Doll K., Harrison N. M., Bush I. J., D'arco P., Llunel M., Causà M. and Noel Y. (2013) *Crystal 2014 User's Manual*., University of Torino, Torino.

Freeman J. J., Wang A., Kuebler K. E., Jolliff B. L. and Haskin L. A. (2008) Characterization of Natural Feldspars By Raman Spectroscopy for Future Planetary Exploration. *Can. Mineral.* **46**, 1477–1500.

Kroll H., Schmiemann I. and von Colln G. (1986) Feldspar solid solutions. *Am. Mineral.* **71**, 1–16. Available at: http://www.minsocam.org/ammin/AM71/AM71_1.pdf [Accessed October 22, 2014].

De La Pierre M., Orlando R., Maschio L., Doll K., Ugliengo P. and Dovesi R. (2011) B3LYP , PBE0 , and WC1LYP) in the Simulation of Vibrational and Dielectric Properties of Crystalline Compounds . The Case of Forsterite Mg 2 SiO 4. *J. Comput. Chem.* **32**, 1775–1784.

Lee C., Hill C. and Carolina N. (1988) into a functional of the electron density f f. **37**.

Maschio L., Kirtman B., Orlando R. and Rèrat M. (2012) Ab initio analytical infrared intensities for periodic systems through a coupled perturbed Hartree-Fock/Kohn-Sham method. *J. Chem. Phys.* **137**, 204113. Available at: http://www.ncbi.nlm.nih.gov/pubmed/23205987 [Accessed October 8, 2014].

Maschio L., Kirtman B., Rérat M., Orlando R. and Dovesi R. (2013) Ab initio analytical Raman intensities for periodic systems through a coupled perturbed Hartree-Fock/Kohn-Sham method in an atomic orbital basis. I. Theory. *J. Chem. Phys.* **139**, 164101. Available at: http://www.ncbi.nlm.nih.gov/pubmed/24181998 [Accessed October 8, 2014].

McKeown D. A. (2005) Raman spectroscopy and vibrational analyses of albite: From 25 C through the melting temperature. *Am. Mineral.* **90**, 1506–1517. Available at: http://ammin.geoscienceworld.org/cgi/doi/10.2138/am.2005.1726 [Accessed October 22, 2014].

Méheut M. and Schauble E. A. (2014) Silicon isotope fractionation in silicate minerals: Insights from first-principles models of phyllosilicates, albite and pyrope. *Geochim. Cosmochim. Acta* **134**, 137–154. Available at: http://linkinghub.elsevier.com/retrieve/pii/S0016703714001021 [Accessed October 22, 2014].

Monkhorst H. J. and Pack J. D. (1976) No Title. **13**, 5188–5192.

Pascale F. (2004) The calculation of the vibrational frequencies of crystalline compounds and its implementation in the CRYSTAL code. *J. Comput. Chem.* **25**, 888–897. Available at: http://onlinelibrary.wiley.com/doi/10.1002/jcc.20019/full [Accessed October 23, 2014].

Prencipe M., Mantovani L., Tribaudino M., Bersani D. and Lottici P. P. (2012) The Raman spectrum of diopside: a comparison between <I>ab initio</I> calculated and experimentally measured frequencies. *Eur. J. Mineral.* **24**, 457–464. Available at: http://openurl.ingenta.com/content/xref?genre=article&issn=0935-1221&volume=24&issue=3&spage=457 [Accessed October 22, 2014].

Prencipe M., Maschio L., Kirtman B., Salustro S., Erba A. and Dovesi R. (2014) Raman spectrum of NaAlSi 2 O 6 jadeite. A quantum mechanical simulation. *J. Raman Spectrosc.*, n/a–n/a. Available at: http://doi.wiley.com/10.1002/jrs.4519 [Accessed October 22, 2014].

Prencipe M., Noel Y., Bruno M. and Dovesi R. (2009) The vibrational spectrum of lizardite-1T [Mg3Si2O5(OH)4] at the point: A contribution from an ab initio periodic B3LYP calculation. *Am. Mineral.* **94**, 986–994. Available at: http://ammin.geoscienceworld.org/cgi/doi/10.2138/am.2009.3127 [Accessed October 22, 2014].

Prencipe M., Noel Y., Civalleri B., Roetti C. and Dovesi R. (2006) Quantum-mechanical calculation of the vibrational spectrum of beryl (Al4Be6Si12O36) at the Γ point. *Phys. Chem. Miner.* **33**, 519–532. Available at: http://link.springer.com/10.1007/s00269-006-0110-1 [Accessed October 22, 2014].

Prencipe M., Pascale F., Zicovich-Wilson C. M., Saunders V. R., Orlando R. and Dovesi R. (2004) The vibrational spectrum of calcite (CaCO3): an ab initio quantum-mechanical calculation. *Phys. Chem. Miner.* **31**, 559–564. Available at: http://link.springer.com/10.1007/s00269-004-0418-7 [Accessed October 8, 2014].

Prencipe M., Scanavino I., Nestola F., Merlini M., Civalleri B., Bruno M. and Dovesi R. (2011) High-pressure thermo-elastic properties of beryl (Al4Be6Si12O36) from ab initio calculations, and observations about the source of thermal expansion. *Phys. Chem. Miner.* **38**, 223–239.

Ribbe P. H. (1983) The chemistry, structure and nomenclature of feldspars. In *Feldspar Mineralogy (Reviews in mineralogy 2)* (ed. Mineral. Soc. Am.). Washington (USA). pp. 1–19.

Smith J. V. (1974) *Feldspar Minerals I. Crystal Structure and Physical Properties.* Springer V., Heidelberg (Germany).

Smith J. V. and Brown V. L. (1988) *Feldspar Minerals. 1. Crystal Structures, Physical, Chemical and Microtextural Properties*. Springer V., Berlin (Germany).

Stangarone C., Prencipe M., Mantovani L., Bersani D., Tribaudino M. and Lottici P. P. (2014) AB INITIO CALCULATED AND EXPERIMENTALLY MEASURED RAMAN SPECTRA OF SPODUMENE (LiAlSi2O6). In *11th GeoRaman International Conference* p. 5061.

Von Stengel M. O. (1977) Normalschwingungen von alkalifeldspaten. *Z. Krist.* **146**, 1–18.

Taylor W. H. (1933) The structure of sanidine and other feldspars. *Z. Krist.* **85**, 425–442.

Tribaudino M., Angel R. J., Cámara F., Nestola F., Pasqual D. and Margiolaki I. (2010) Thermal expansion of plagioclase feldspars. *Contrib. Mineral. Petrol.* **160**, 899–908. Available at: http://link.springer.com/10.1007/s00410-010-0513-3 [Accessed March 20, 2014].

Wu Z. and Cohen R. (2006) More accurate generalized gradient approximation for solids. *Phys. Rev. B* **73**, 235116. Available at: http://link.aps.org/doi/10.1103/PhysRevB.73.235116 [Accessed October 18, 2014].

Captions of figures

Fig. 1: Albite structure (*left*: *c* axis projection; *right*: *b* axis projection) obtained by the single-crystal X-ray structure refinement of the studied sample. The red tetrahedra contain silicon, the green ones aluminum, Na^+ atoms are shown in yellow. The four non-equivalent tetrahedra are labeled as $T_1(0)$, $T_1(m)$, $T_2(0)$ and $T_2(m)$. The two types of oxygens (O_{A1} and O_{A2}) are shown too.

Fig. 2: Raman tensor XYZ axes with respect to the triclinic crystallographic cell (*a b c* crystallographic axes).

Fig. 3: Experimental averaged Raman spectrum of albite (in gray) compared with the simulated spectrum (in black) for polycrystalline isotropic powder, calculated at 632.8 nm wavelength and 300 K.

Fig. 4: Calculated Raman spectra of albite for the six different polarization configurations (in black) compared with the experimental data (in grey). Each measured spectrum is scaled so that the intensity of the strongest peak agrees with the theoretical intensity of the corresponding calculated mode.

Fig.5: Eigenmode plots for four characteristic peaks in the Raman spectrum of albite: modes at 290 and 513 cm^{-1} are shown on *ac* plane, whereas modes at 485 and 825 cm^{-1} are displayed on *ab* plane. Atom displacements are indicated by black arrows. Atom types are: Na (yellow), Si (red), Al (green) and O (blue).

Fig. 6: Calculated isotopic shift of the wavenumbers of albite when Na (lower panel) or Al (middle panel) mass is increased by ~ 20%. In the upper panel is reported the percentage contribution of Si, calculated from its different isotopic shifts in the three occupied atomic position (Taylor, 1933).

Tables

Table 1: Chemical analyses by SEM-EDS. *Or* stands for orthoclase, *Ab* for albite, *An* for anorthite

	Avg.	2σ
SiO_2 wt%	67.88	0.84
Al_2O_3	19.39	0.40
CaO	0.19	0.10
Na_2O	11.35	0.26
K_2O	0.32	0.10
Total	99.13	1.24
Si *apfu*	2.99	0.02
Al	1.01	0.01
Ca	0.009	0.004
Na	0.97	0.01
K	0.02	0.01
Σ cations	5.00	0.06
Σ *T* site	4.00	0.03
Or %	1.79	0.49
Ab	97.30	0.86
An	0.91	0.44

Table 2: Single-crystal XRD experimental and calculated unit-cell parameters of low albite (in Calculated, (a): static values; (b): values at 300 K). Calculated (b) *vs* experimental % differences are also reported.

	Experimental	Calculated		% Differences
		(a)	(b)	
a (Å)	8.1395(5)	8.1745	8.2199	1.0
b (Å)	12.7838(7)	12.8510	12.8604	0.6
c (Å)	7.1597(6)	7.2075	7.2136	0.8
α (°)	94.242(6)	94.306	94.278	0.04
β (°)	116.590(7)	116.775	116.547	-0.04
γ (°)	87.674(5)	87.791	87.646	-0.03
V (Å^3)	664.35(9)	674.06	680.23	2.4

Table 3: Comparison between calculated and experimental Raman shifts. Experimental data are: from McKeown (low albite) and from Freeman (low albite, *first column*; high albite, *second column*). Wavenumbers are in cm^{-1}. Calculated Raman intensities *I* are normalized to the most intense peak at 513 cm^{-1} and refer to the experimental conditions $T = 300$ K, $P = 1$ atm and $\lambda = 632.8$ nm on powder (polycrystalline isotropic intensities). Measured Raman wavenumbers are obtained by peak fitting procedure through LABSPEC 5.78.24, Jobin Yvon/Horiba, software package. Differences $\Delta\nu$ are with respect to our calculated data. N_{exp} is the total number of Raman wavenumbers; $\overline{\Delta\nu}$, $\overline{|\Delta\nu|}$ and $|\Delta\nu|_{max}$ are the mean difference, the mean absolute difference and the absolute maximum difference evaluated over the set of N_{exp} peaks, respectively.

			Experimental							
	Calculated		This work		McKeown[27]		Freeman[29]			
Mode #	ν	*I*	ν	Δν	ν	Δν	ν	Δν	ν	Δν
1	66	0.11	63	3.4	67	-0.6				
2	73	0.23	72	1.1						
3	92	0.13	86	5.6	89	2.6				
4	118	0.20	112	5.6	111	6.7				
5	148	0.13	144	3.9	140	7.9	140	7.9		
6	151	0.15	149	1.6	150	0.6				
7	161	0.35	162	-1.3	160	0.7			156	4.7
8	168	0.13	169	-0.7	168	0.4				
9	176	0.04	179	-3.1						
10	187	0.57	185	2.0	183	4.1	186	1.1	182	5.1
11	207	0.37	208	-1.0	207	0.0	209	-2.0	206	1.0
					216					
12	254	0.08	251	3.6	250	4.5	252	2.5	254	0.5
13	271	0.25	269	1.8	268	2.9	269	1.9	266	4.9
14	290	0.57	290	0.0	289	0.8	291	-1.2	287	2.8
15	310	0.06	308	2.3	307	3.3				
16	329	0.10	328	1.4	327	2.3	329	0.3	327	2.3
17	350	0.05	353	-3.4	346	3.6	349	0.6	346	3.6
					346					
					367					
18	398	0.05	398	-0.5	396	2.0	400	-2.0	399	-1.0
19	410	0.07	407	2.5	406	3.5	408	1.5	406	3.5
20	419	0.09	416	2.9			416	2.5		
21	466	0.07	456	10.1	455	11.1	457	9.1	452	14.1
22	485	0.82	478	6.5	477	7.8	479	5.8	476	8.8
23	492	0.02	494	-1.6						
24	513	1.00	507	6.8	505	8.5	507	6.5	507	6.5
					528					
25	579	0.03	578	0.3	578	0.8	580	-1.2	578	0.8
26	634	0.01	632	1.6	632	1.9	634	-0.1	636	-2.1
27	649	0.04	646	2.8	645	4.1	646	3.1	651	-1.9
28	724	0.01	720	4.3	720	4.5	721	3.5	737	-12.5
					720					
29	768	0.22	763	5.3	762	6.5	764	4.5	762	6.5

30	784	0.02	776	8.1						
31	825	0.14	815	10.3	814	11.0	815	10.0	812	13.0
32	972	0.05	978	-6.2	977	-5.4	978	-6.4	977	-5.4
33	1001	0.02	1006	-5.0	1005	-3.8	1008	-6.8		
34	1012	0.04	1014	-1.8			1013	-0.7		
35	1037	0.04	1032	4.6	1030	6.8	1033	3.8	1030	6.8
36	1044	0.01	1046	-1.5	1046	-1.5	1046	-1.5		
37	1102	0.20	1100	1.7	1098	3.7	1099	2.7	1098	3.7
38	1117	0.10	1115	2.1	1116	1.0	1113	4.0	1106	11.0
39	1156	0.01	1152	4.2	1151	5.0	1152	4.0	1139	17.0
					1170					
		N_{exp}	39		39		28		24	
		$\overline{\Delta\nu}$	2.1		3.2		1.9		3.9	
		$\overline{\lvert\Delta\nu\rvert}$	3.4		4.1		3.5		5.8	
		$\lvert\Delta\nu\rvert_{max}$	10.3		11.1		10.0		17.0	

Table 4: Comparison between the frequencies of the main Raman features of albite samples with different compositions. Wavenumbers are in cm^{-1}. *Or* stands for orthoclase, *Ab* for albite, *An* for anorthite, *Cn* for celsian, *Sr-Fsp* for feldspar with Sr.

This work	McKeown	Bendel and Schmidt	Freeman et al.						
		San0	JDP Albite	JDP#10-997	ASU BUR3460A	JDP 109940	EPSc#313-4	EPSc#313-10	AW#162
$Or_{1.79}Ab_{97.3}An_{0.91}$		$Or_{0.6}Ab_{97.4}An_{0}Cn_{1.6}Sr\text{-}Fsp_{0.4}$	$Or_{0}Ab_{100}An_{0}$	$Or_{2.2}Ab_{85.92}An_{11.88}$	$Or_{0.48}Ab_{99.39}An_{0.13}$	$Or_{0.57}Ab_{98.82}An_{0.61}$	$Or_{0.76}Ab_{98.4}An_{0.9}$	$Or_{1.34}Ab_{97.91}An_{0.75}$	$Or_{0.35}Ab_{93.66}An_{5.99}$
Minas Gerais (Brazil)	Amelia, Rutherford Mine (Virginia)	Synthetic sample	Amelia, Court House (Virginia)	Eganville, Ontario (Canada)	Keystone, South Dakota	Lake George, Colorado	Meconite, New York	St. Gothard, Switzerland	Haicheng, Liaoning, China
144	140	142.3							
185	183		186	184.8	185.6	184.1	185.3	186.4	185.9
290	289		290.9	290.5	291	290.1	289.7	291	290.7
456	455	467	457	457.8	458.3	461.2	455.9	457.3	457.8
478	477	479	479.4	479.2	479.3	479.3	479.1	479.4	479.7
507	505	510.2	507.6	507.8	507.7	507.6	507.7	507.9	507.7

Table 5: Comparison among three sets of calculated wavenumbers (cm^{-1}) Raman features of low albite. In bold are reported bands assigned as overtone modes in McKeown (2005). The correspondence between the calculated data is based on a comparison with the experimental data.

McKeown	Méheut and Schauble	This work
LD	DFT (PBE)	HF/DFT (WC1LYP)
ν	ν	ν
	60	
69	73	66
		73
73	88	92
120	111	118
135	144	148
147	147	151
162	158	161
172	166	168
	176	176
189	181	187
201	202	207
221		
242	244	254
278	259	271
295	278	290
306	298	310
317	315	329
344	333	350
349		
362		
400	380	398
405	390	410
414	397	419
460	436	466
478	456	485
	460	492
506	481	513
526		
578	550	579
627	600	634
633	617	649
725	688	724
728		
764	727	768
770	737	784
797	778	825
962	926	972

994	957	1001
1010	966	1012
1032	987	1037
1056	1001	1044
1099	1052	1102
1111	1067	1117
1159	1108	1156
1173		